

Capillary penetration failure of blood suspensions

Ronghui Zhou, Hsueh-Chia Chang *

Department of Chemical and Biomolecular Engineering, University of Notre Dame, 182 Fitzpatrick, Notre Dame, IN 46556, USA

Received 24 August 2004; accepted 8 February 2005

Available online 17 March 2005

Abstract

Blood suspension fails to penetrate a capillary with radius R less than $50\ \mu\text{m}$ even if the capillary is perfectly wettable. This invasion threshold is attributed to three red blood cells (RBCs) segregation mechanisms—corner deflection at the entrance, the intermediate deformation-induced radial migration and shear-induced diffusion within a packed slug at the meniscus. The shear-induced radial migration for deformable particles endows the blood cells with a higher velocity than the meniscus to form the concentrated slug behind the meniscus. This tightly packed slug has a higher resistance and arrests the flow. Rigid particles and rigidified blood cells result in wetting behavior similar to that seen for homogeneous liquids, with decreased RBC migration towards the capillary centerline and reduction of packing. Corner deflection with a radial drift velocity accelerates the radial migration for small capillaries. However, deformation-induced radial migration is the key mechanism responsible for penetration failure. This sequence of mechanisms is confirmed through videomicroscopy and scaling theories were applied to capture the dependence of the critical capillary radius as a function of RBC concentrations.

© 2005 Elsevier Inc. All rights reserved.

Keywords: Suspension rheology; Diagnostic kits; Blood rheology

1. Introduction

Development of miniature blood diagnostic kits has seen a great deal of interest recently. Many of these kits, involving multistage separation and detection, require the blood sample to be transported through a network of microchannels. Capillary wetting is by far the most common blood transportation mechanism in diagnostic kits. A portion of the blood sample invades into a microneedle or glass capillary that leads into an enclosed kit [1]. The entire drop cannot penetrate through the kit as the back meniscus would suppress the penetration. Since the volume of blood sample has a strong effect on the marketability of the kit, considerable effort has been focused on making the smallest microfluidic kit and loading microneedle that require the least amount of blood sample.

However, recent reports show that whole blood cannot penetrate far into a wetting capillary or microneedle with

diameter smaller than $100\ \mu\text{m}$. This has hence become a major technical obstacle to further miniaturization of diagnostic kits. As the red blood cell (RBC) dimension is only ten microns, it is unlikely that this penetration failure is due to RBC blockage. The most likely cause of the penetration failure is a RBC aggregation mechanism that can locally increase the RBC concentration to maximum packing. As the blood suspension viscosity is a strong function of the RBC concentration, the hydrodynamic resistance at maximum packing becomes too high to allow further penetration.

There are numerous suggested and known suspension segregation phenomena that could lead to RBC aggregation. Particles are known to migrate across streamlines due to asymmetry [2], deformability [2,3], inertia [4] and particle–particle interaction [5]. The first three mechanisms give rise to cross-streamline drift or ballistic motions whereas the last produces transverse diffusion-like migration mechanisms, as collision theories often do.

Another known aggregation phenomenon is the packing of particles behind an advancing meniscus [6]. This will be shown to be an important mechanism in the penetration

* Corresponding author. Fax: +1 574 631 8366.
E-mail address: chang.2@nd.edu (H.-C. Chang).

failure. However, as shown by Karnis and Mason [6], such packing is negligible for rigid latex particles and there is insignificant change in the meniscus wetting speed from that of a homogeneous suspension. The packing must hence be more pronounced for RBCs for a yet unknown reason.

In this report, we shall show that the key mechanism for penetration failure of small capillaries is cross-streamline migration due to particle deformation. It is the deformation driven radial migration that prevents the RBC from rehomogenizing beyond the entrance region-like rigid particles. Additionally, Fahraeus–Lynquist effect of a radially segregated blood suspension with a marginal layer of RBC depleted region near the capillary wall can only occur for deformable RBCs. Due to the negative diffusion driven by deformation-induced radial migration, the RBCs favor the capillary axis and preferentially sample the higher velocity there. As a result, they are endowed with a higher average velocity than the average liquid velocity, which is also the meniscus velocity. The RBCs then outrace the meniscus and pack behind it to form a highly concentrated slug. When the concentration within the slug reaches maximum packing, the penetration advance is arrested. We document all these mechanisms with video imaging and verify them with scaling theories that collapse our data.

2. Wetting and colloid segregation theory

Penetration of a wetting fluid into a circular capillary by Poiseuille flow is known to advance at a speed of $\langle u \rangle = \sigma R / (8L\mu)$, which scales linearly with the capillary radius R and inversely with the wetted capillary length L [7]. Experiments show that the speed for typical whole blood surface tension ($\sigma = 55.89 \times 10^{-3}$ N/m) [8] and viscosity ($\mu = 4$ cp) is still a robust 1.0 cm/s at a distance of $L = 1.0$ cm from the entrance of a capillary with $R = 25$ μm . Such homogeneous wetting would persist till $R \sim 5$ μm when each individual blood cells would need to be compressed before they can enter the capillary. Hence, penetration failure at $R \sim 50$ μm must be due to a blood cell segregation phenomenon that can somehow produce a concentrated slug within the capillary.

The most plausible segregation mechanism is related to the Fahraeus–Lynquist phenomenon [9] of radial blood cell segregation in the unidirectional flow of a straight capillary, when the flow is not driven by wetting but by a continuous flow driven by a syringe or a higher pressure head. Fahraeus–Lynquist segregation of RBCs in unidirectional capillary flow has been attributed to a variety of mechanisms [2–5] due to asymmetry, deformability and inertia. Migration due to asymmetry, deformability, or inertia is usually attributed to hydrodynamic interaction between the particle and a flat wall with unidirectional shear flow. Typically, these mechanisms break the fore–aft symmetry of the flow field around the particle to produce a privileged orientation that couples

with a net hydrodynamic drag force in the cross-streamline direction to produce drift away from the wall. The asymmetric velocity perturbation produced by a nonspherical particle in the presence of wall contributes to this drift [2]. For particles with fore–aft symmetry and without a fixed orientation, like RBCs, external flow will only result in zero-mean rotation and hence no net transverse hydrodynamic force or drift. It is the small deformation produced by the strain of external flow that breaks the fore–aft symmetry and the compressive and tensile forces normal to cell surface will result in a net transverse force and migration [3]. Inclusion of inertia is sufficient to break the symmetry of the velocity field around the particle. Such flow field around a particle near a wall differs from the velocity field of a particle in an unbounded flow. The extra inertial drag and compressive force due to the wall lead to a transverse migration with velocity $81Ua\gamma^{1/2}/6\pi\nu^{1/2}$ [4]. If the particle is spherical and rigid, only the inertial mechanism can produce a cross-streamline drift away from a flat wall. However, rigid particles ten microns in radius equilibrate with the fluid velocity within a negligible inertial time of $\sim 10^{-5}$ s and inertial effects are typically discounted. For curved flows near a nonplanar surface, normal stress instead of tangential drag can push a spherical particle across streamlines. Fore–aft symmetry along the streamline is also revoked by the curved streamline and drift exists even for spherical particles. The resulting normal stress gradient across streamline can be expressed as a normal pressure gradient by Faxen Law [10]. El-Kareh and Secomb [11] have analyzed such cross-streamline deflection around a cylinder and concluded that, for a cylinder much larger in radius than the particle radius, the deflection is negligible.

There are three known particle–particle interaction theories for suspension diffusion—all for simple unidirectional shear flows. One drives the particle from a high shear-rate streamline to a low shear-rate streamline and is commonly known as shear-induced migration [5]. The basic mechanism is that there is more collision on the high-shear part of the particle—it is a finite-size effect. Hence, a normal gradient of the tangential shear-rate, i.e., a normal curvature in the tangential velocity, must be appreciable over the particle dimension a . Its diffusivity scales as $\gamma\phi a^2$ as the collision frequency is $\gamma\phi$. It is a negative diffusivity as the diffusion is towards lower shear rates. The second diffusive mechanism across streamlines is due to normal concentration gradient across the particle, which also produces a change in the collision frequency across the particle. Yet a third mechanism corresponds to a shear-rate gradient produced by viscosity gradient. These two mechanisms also have a diffusivity scaling of $\gamma\phi a^2$ but it is a positive diffusivity since the diffusion is down the concentration gradient. The characteristic diffusion time across a capillary is hence $R^2/\gamma\phi a^2$ and for wetting flow, the capillary length over which this occurs is the longitudinal induction length $L_t = \langle u \rangle R^2/\gamma\phi a^2 = (R^3/a^2)/\phi$ for radial segregation to develop at the entrance.

The cross-streamline migration mechanisms are believed to cause the famous Fahraeus–Lynquist effect—the radial segregation of blood cells inside capillaries and the attendant change in the local blood cell concentration. However, which cross-streamline mechanism is responsible has not been scrutinized and will be analyzed in this report. Moreover, the radial segregation of blood cells is towards the capillary axis and hence would reduce the effective viscosity of the blood suspension. Hence, these radial migration mechanisms by themselves cannot explain the penetration failure of blood suspension.

3. Experiments

The capillary wetting system used in this study is depicted in Fig. 1. It consists of a glass capillary tube of known radius (Polymicro Technologies, Phoenix, AZ), a microscope and high speed video camera system (Olympus 2004). A series of capillary wetting experiments are then

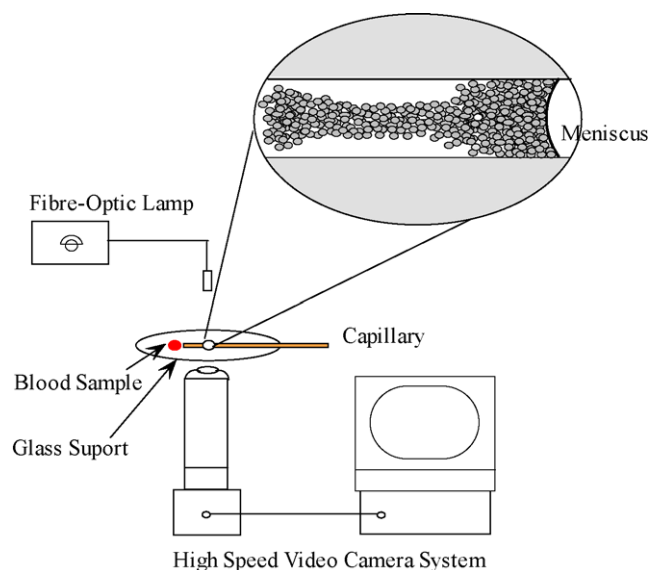


Fig. 1. Schematics of wetting experiment setup.

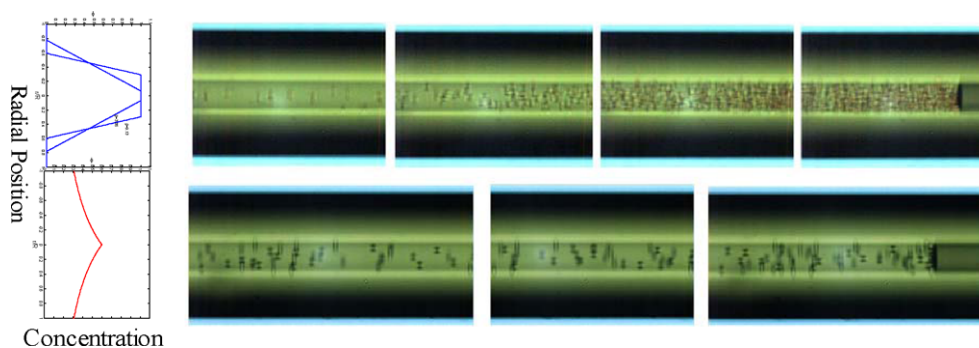


Fig. 2. Blood (top) and latex (bottom) suspensions (both $\phi_0 = 1\%$) advancing in capillary. In blood suspension (top), a concentrated slug is formed behind the meniscus but blood cells are segregated towards the axis behind the slug. For latex suspension (bottom), neither meniscus packing nor upstream segregation is observed. The concentration profiles on the left are computed profiles for deformable particles and rigid particles at two characteristic conditions, $\phi_0 = 0.01$, $\phi = 3.86$, along the capillary and for rigid particles.

carried out by placing a drop (volume 100 μL) of bovine RBC suspension or latex suspension at the entrance of the glass capillary whose radius R ranges from 10.5 to 50 μm . All suspensions are deemed to wet the glass capillary from static angle measurements on glass substrates. The meniscus motion and the particle concentration are monitored with the high speed video camera (1000 frames/s) attached to a microscope. The field of view contains roughly a 200 μm section of the capillary and video movies are recorded at 6–10 separate stations of known distances from the entrance. A separate experiment is carried out for measurement and imaging at each station for a given R , ϕ_0 and drop volume placed at the capillary entrance.

Bovine RBCs (Animal Technologies, Inc., Tyler, TX), were resuspended in standard 0.9% saline solution (Phoenix Scientific, Inc., St. Joseph, MO) to prepare blood suspensions of different concentration. The initial erythrocytes volume fraction was determined to be roughly 95–100% by measuring the hemoglobin concentration. The RBCs were diluted, respectively, to 1, 5, 10, 20, 30, 40% blood suspensions. A 5 μm polystyrene Flux latex particle suspension, whose particles are roughly the size of erythrocytes, was also used at $\phi_0 = 1$ and 5% to contrast the behavior of rigid particles to deformable ones. Glutaraldehyde treated RBCs, reported as rigidified RBCs [12], were also prepared by reaction of 25% glutaraldehyde with RBCs at a 2:1 molar ratio with RBC haemoglobin concentration. Glutaraldehyde treated RBCs were then washed and resuspended in standard 0.9% saline solution to prepare $\phi_0 = 10$ solution.

The recorded images of meniscus advancing show a concentrated slug behind the meniscus of deformable blood suspension, yet not behind the latex particle suspension (Fig. 2). The deformable RBCs behind the slug have clearly aligned themselves to the axis (top left) and their concentration is distinctly lower than that at the slug (top right). In contrast, latex particles are radially unsegregated and their concentration is homogeneous throughout the slug. The slug length L_{slug} does not vary significantly downstream at low concentrations ($<10\%$) and small capillary radius, but its value is a strong increasing function of the capillary radius (Fig. 10,

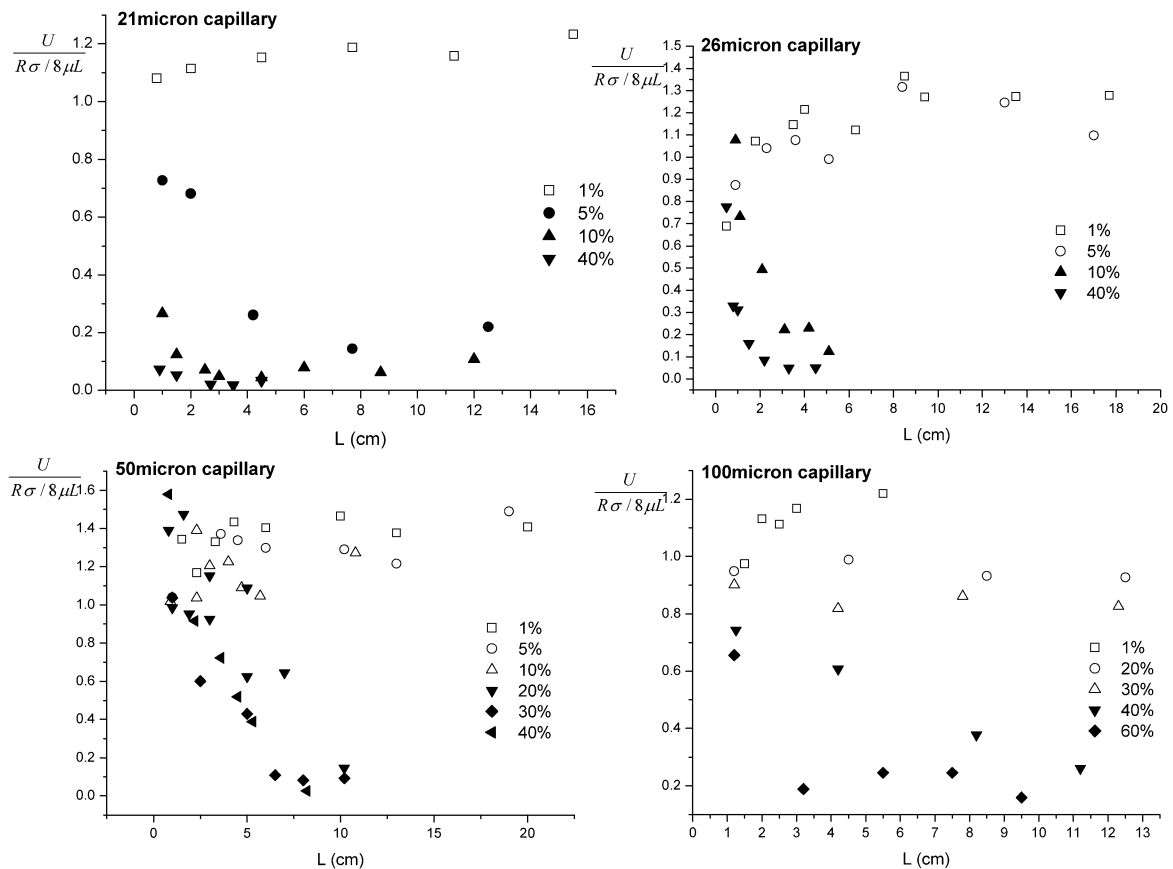


Fig. 3. Scaled meniscus velocity versus the wetted length L . The precipitous drop in the velocity within 1 cm from the entrance for concentrations beyond the critical one is evident for each of the three capillaries used.

insert). The meniscus curvature also remains constant during the penetration, suggesting that the RBCs in the concentrated slug have not embedded themselves onto the interface and caused possible changes in the surface tension. At low concentrations, the segregated RBCs behind the slug can be visually observed to migrate into the slug.

While the concentration of RBC in slugs is observed for all conditions, the wetting dynamics depart from homogeneous wetting only for high concentration ϕ_0 and low radius R . Measured meniscus speeds of blood suspension in capillaries of varying radius R and ϕ show a precipitous drop at concentration $\phi_0 = 40\%$ for $R = 25 \mu\text{m}$ capillary, $\phi_0 = 10\%$ for $R = 13 \mu\text{m}$, and $\phi_0 = 5\%$ for $R = 10.5 \mu\text{m}$, respectively. In Fig. 3, the recorded meniscus velocity $\langle u \rangle$ is normalized by the homogeneous scaling to be $8\langle u \rangle \mu L / R\sigma$ and is shown to be close to the theoretical value of unity for small ϕ_0 and large R . For the other values, $\langle u \rangle$ drops precipitously over a short distance of approximately 1 cm from the entrance. This anomalous wetting behavior is believed to explain why whole blood cannot penetrate far into a capillary with $R < 25 \mu\text{m}$. To further establish that the RBC deformability is responsible for penetration failure, we use the glutaraldehyde treated RBCs as a control and compare the meniscus velocity of the untreated blood suspension to this control in Fig. 4. At the critical concentration of 26 μm

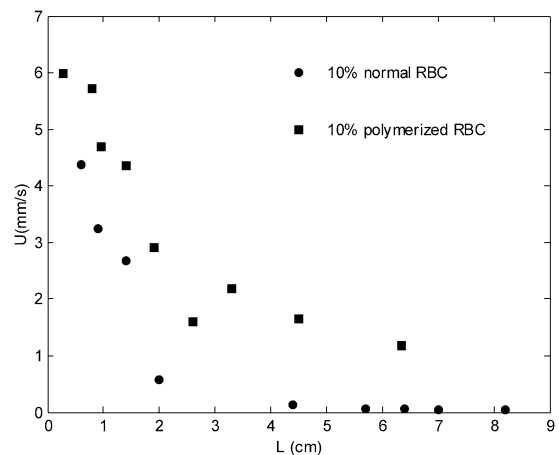


Fig. 4. Velocity difference between normal RBC suspensions and glutaraldehyde treated RBC suspensions at critical concentration 10% of a 26 μm capillary.

capillaries, the rigidified 10% blood suspension invades with a higher velocity than the untreated blood suspension at different positions along the capillary.

Capillaries less hydrophilic are prepared by pumping corn oil through for perfusion. The residual liquid inside is removed by connecting one end of the glass capillary with a vacuum and checked under microscope prior to use. The sur-

face modified capillaries showed a noticeable change both in contact angle and in the magnitude of meniscus velocity (Fig. 5). The less hydrophilic capillaries demonstrated a negligible longitudinal concentration gradient compared with blood suspensions due to the reduced difference of the radial velocity.

The corner deflection mechanism is scrutinized in separate experiments with a simple reservoir setup. A diamond cutter is used to keep the uniformity of each capillary corner. Samples to be analyzed, both blood and latex suspensions are withdrawn from inside the reservoir through the capillary. The corner of the withdrawing capillary is observed under the high speed camera and particle evolutions at different withdrawing flow rates are recorded.

In the corner deflection experiments, as demonstrated in Fig. 6, both the RBCs and latex particles are clearly deflected across the liquid streamlines and away from the capillary corner wall. They are then injected along the capillary axis in a single file or within a small cylindrical core around the axis. The same deflection trend shown by both RBCs and latex particles indicates that deformation or asymmetry is not the key factor for these phenomena. The deflected distance is also insensitive to shear rate and flow rate, as the three images in Fig. 6 correspond to velocities separated by two orders of magnitude. The particle inertial equilibration time $m/6\pi\mu a$ is about 10^{-5} s while the transit time of the particles around the corner is longer than 10^{-2} s. Hence it is unlikely that inertia plays a role. Collision is also ruled out from visual observation. A conic suspension structure develops at the entrance due to the deflection, as shown in Fig. 7. The suspension within the cone is more concentrated and the RBCs are injected within a larger core around the capillary axis at higher velocities. This larger injected core at high velocities is probably due to enhanced particle collision in the highly packed conic region. We have attempted to mechanically alter the sharpness and capillary wall thickness of the capillary. Regardless of the jaggedness of the corner (as evident in Fig. 6), the corner deflection phenomenon is always observed.

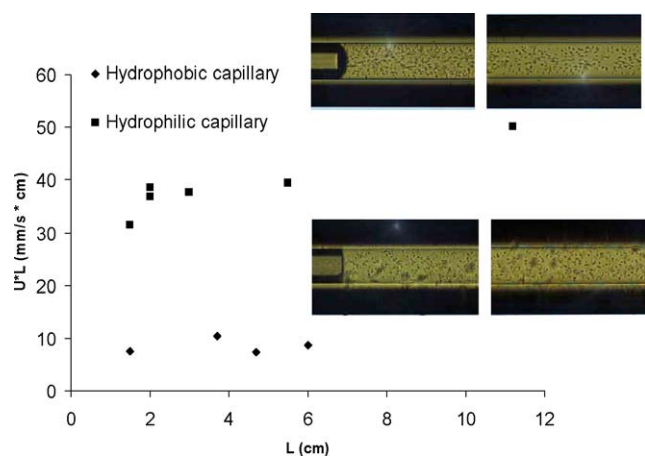


Fig. 5. Meniscus velocity of both hydrophilic capillary (top image) and hydrophobic capillary (bottom image).

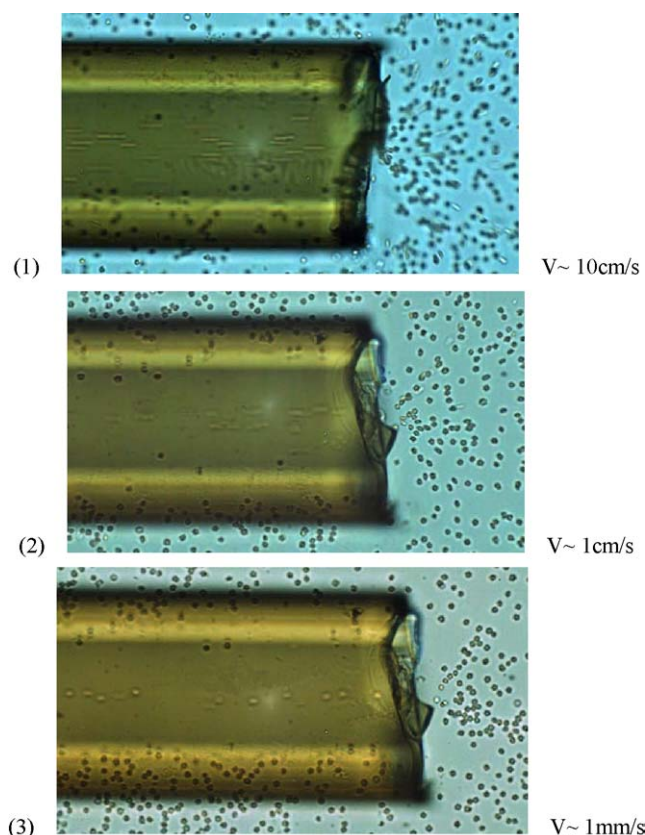


Fig. 6. Corner deflection of blood cells at three invasion velocities of roughly 10, 1 cm/s and 1 mm/s produced by a syringe pump. Note the deflected distance is independent of the velocity over a velocity range that spans three orders of magnitude, as is consistent with our theory.

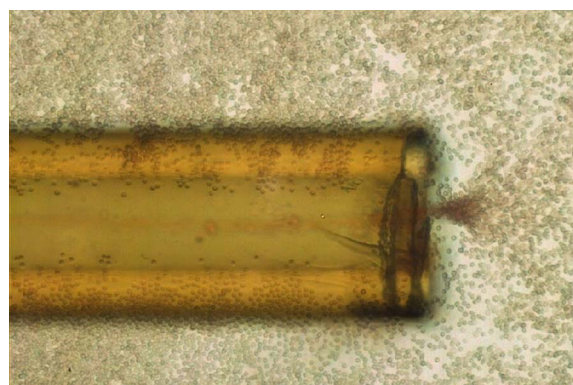


Fig. 7. Corner deflection and cone formation of blood cells at the entrance of capillaries with $R = 50 \mu\text{m}$ and $\phi_0 = 1\%$.

All of these observations suggest a mechanism for the anomalous wetting dynamics involving a sequence of segregated, homogenization and packing dynamics for the blood cells. As the RBCs segregate and migrate to the axis due to corner deflection, they achieve a higher average velocity than a homogeneous suspension, i.e., the average fluid velocity $\langle u_{\text{fluid}} \rangle$. After this entrance transit region, there is an intermediate well segregated region due to shear-induced migration of deformable RBCs. As the meniscus must move

at the average fluid velocity $\langle u_{\text{fluid}} \rangle$ due to flow balance, the RBCs reach the meniscus and pack behind it to form the concentrated and radially unsegregated slug region. The slug concentration increases in time at a rate proportional to the flux from the segregated region and hence increases with ϕ_0 .

As the suspension viscosity is known to reach extremely high values [13] when the blood cell concentration reaches maximum packing ϕ_{max} , viscous drag at the slug increases as the meniscus advances. However, viscous dissipation within the slug can only affect the wetting dynamics if the slug length L_{slug} is comparable to L . This occurs at small speeds and small R . These qualitative arguments for the anomalous wetting dynamics occurring at large ϕ_0 and small R are quantified with a scaling model (see below) to determine the critical radius R_c as a function of ϕ_0 .

4. Intermediate segregated region and the Fahraeus–Lindquist effect

The radial migration of deformable RBCs towards the axis, responsible for the Fahraeus–Lindquist effect, is clearly also evident in blood penetration, as seen in Fig. 2. Without this migration, collision will rehomogenize the particles radially after the corner segregation, as seen in the latex particle images of Fig. 2. A radial migration model for deformable drops has been suggested by King and Leighton [14], which combines the deformation term derived by Chan and Leal [15] with a term that combines shear-induced migration and self-diffusion [3,16] to produce the radial particle flux for a radially distributed blood cell volume fraction $\phi(r)$,

$$N_r = k_d \left(\gamma a \frac{\mu}{\sigma_{\text{cell}}} \right) \gamma a (ar) / (R^2) \phi - D \frac{\partial \phi}{\partial r}, \quad (1)$$

where k_d is a universal constant, a is the particle (blood cell) radius, σ_{cell} is the effective membrane tension and γ is the local shear rate. The shear rate γ has a characteristic value of $\langle \gamma \rangle = \langle u \rangle / R$ for a capillary.

The first term is due to shear-induced migration of a deformable particle and it scales as γ^2 . The second term with a diffusion coefficient $D = \lambda \gamma a^2 \phi$, where λ is another constant, measures diffusion down concentration gradients due to particle–particle interaction, including contributions from both self-diffusivity and gradient-induced drift. In contrast, the shear-induced migration rate for a rigid particle is $\gamma a^2 \phi$ and has the same linear scaling as the second diffusion term. As a result, since the steady radial ϕ distribution in well-developed capillary flow is determined by $N_r = 0$, the rigid particle concentration profile and apparent viscosity are independent of γ or R as both terms in N_r have identical scaling for γ . For deformable particles, however, the scaling with respect to γ is different for the two terms in N_r and the ratio between the two yields a unique parameter,

$$\beta = (2k_d / 9\lambda\sigma_{\text{cell}})(a\Pi R / \phi_0), \quad (2)$$

which specifies the degree of segregation of the RBCs and the resulting change in apparent viscosity. We take King and Leighton's empirical value of $\lambda = 0.3$, k_d is subsequently fitted to be -0.012 and σ_{cell} , the effective tension of RBC, is taken to be 4×10^{-4} mN/m from the AFM force measurements of Tachev et al. [17]. The pressure gradient Π is the pressure gradient of a particular flow channel that can also be deduced from the flow rate if a homogeneous fluid is assumed. It is related to the characteristic shear rate γ through force balance.

In contrast, the radial flux for rigid particles is

$$N_r = -k_c a^2 \left(\phi^2 \frac{\partial \gamma}{\partial r} + \phi \gamma \frac{\partial \phi}{\partial r} + \delta \phi^2 \gamma (d \ln \mu / d \phi) \frac{\partial \gamma}{\partial r} \right), \quad (3)$$

where the third term accounts for viscosity gradient with $\delta = 1.52$, and the first two capture the usual shear-rate and concentration gradient mechanisms.

Due to the identical scaling for all three terms in (3), the equation is exactly integrable. The first integral yields a power law scaling

$$(\phi^*(r) / \phi_w) = (\gamma_w / \gamma(r)) (\mu_w / \mu(\phi^*(r)))^{\delta \nu} \quad (4)$$

if a power law constitutive equation for the viscosity is used:

$$\mu(\phi) = \mu_{\text{fluid}} (1 - (\phi / \phi_m))^{-\nu}. \quad (5)$$

The quantities in (4) with subscript w correspond to wall values, which are taken as reference points.

Equation (4) can be substituted into the equation of motion, driven by a constant pressure gradient Π ,

$$\frac{1}{r} \frac{\partial}{\partial r} \left(\mu(\phi^*) \frac{\partial u}{\partial r} \right) = \Pi. \quad (6)$$

The viscosity dependence on concentration $\mu(\phi^*)$ is typically different for blood cells and rigid particles. Suspension of rigid particles reaches infinite viscosity at the simple cubic packing volume fraction of $\phi_m = 0.62$ while blood cells can be squeezed considerably before the viscosity blows up. However, as we shall confirm that for blood cell volume fraction below 0.6, the value of the critical concentration is unimportant and is taken to be $\phi_m = 1.1$. The plasma viscosity μ_{fluid} in (5) is taken to be 1.0 cp and the exponent $\nu = 1.82$ will be shown to adequately fit the data of Haynes and Burton [13].

Inserting (4) into (6) and solving for u in a cylindrical capillary, produces the shear-rate and concentration profiles. Fluid and particle flux balances then specify the flow rate and the reference wall values,

$$(1 - \phi_0) Q = \int_0^R (1 - \phi^*(r)) u(r) r dr, \quad (7a)$$

$$\phi_0 Q = \int_0^R \phi^*(r) u(r) r dr, \quad (7b)$$

where ϕ_0 is the homogeneous concentration and Q the flow rate.

Due to the self-similar scaling of (4), a universal relationship between $\phi^*(r)/\phi_0$ and r/R can be obtained

$$(\phi^*/\phi_0)(r/R) = \xi (1 - (\phi_0/\phi_m)\phi^*/\phi_0)^{\delta\nu-\nu}, \quad (8)$$

where the exponent $(\delta - 1)\nu \sim 0.94$ for the value $\delta = 1/0.66$ and $\nu = 1.82$ of our constitutive equation. Since $(\delta - 1)\nu$ is close to unity, (8) can be simplified to an explicit universal distribution for rigid particles,

$$(\phi^*(r)/\phi_0) = \xi / (\xi\phi_0/\phi_m + r/R), \quad (9)$$

where $\xi = \phi_w / (1 - \phi_w/\phi_m)$ and $\phi_w(\phi_0)$ is determined from both particle and liquid flux balance and is only a function of ϕ_0 . For given homogeneous concentration (1% particle volume fraction), this distribution could be integrated numerically to produce the profiles as shown in Fig. 2. This universal distribution also produces an apparent viscosity that depends only on ϕ_0 , the homogeneous concentration,

$$\mu_{\text{rigid}}^{\text{app}} = \pi \Pi R^4 / 8Q = \phi_0 \pi \Pi R^4 / \left(8 \int_0^R \phi^*(r)u(r)r dr \right). \quad (10)$$

Hence, the apparent viscosity for rigid suspension is independent of capillary radius—a scale-invariant universality due to the identical scaling of the three migration mechanisms due to particle interaction in (3). The equilibrium profile (9) only slightly favors the axis. From an entrance distribution localized at the axis due to the corner deflection, rigid

particles quickly rehomogenize by particle–particle interaction to reach the nearly homogeneous distribution of (9). The ‘induction’ period for this equilibrium is $R^2/\gamma a^2\phi$ and the induction length is $R^3/a^2\phi$. For a 10 μm particle solution at $\phi = 0.4$ and $R = 20 \mu\text{m}$, this distance is less than 0.2 mm. This is shorter than the penetrated distance when invasion failure occurs for a similar blood suspension in Fig. 3. It would have equilibrated and homogenized at that distance and could not have caused penetration failure.

For deformable particles, the equilibrium distribution must be determined with a simultaneous solution of the radial flux equation (3) with the equation of motion (5). As the scaling of the deformation mechanism in (1) is different from the diffusion mechanism, a universal distribution like (9) is impossible. Instead, the normalized distribution (ϕ^*/ϕ_0) is a function of (r/R) and the only parameter β of (2).

We have obtained these profiles as a function of β by solving the flux equation (1) and the equation of motion (4) simultaneously. We find that a clear plasma layer develops at $\beta_c = 15/7$.

The apparent viscosity is also a function of β . In Fig. 8, we compose our computed viscosity as a function of R to measured values for continuous through flow at constant Q for blood suspensions of different volume fractions [18]. Satisfactory agreement is observed. In particular, the locus of critical β for marginal layer is also shown and is in agreement with experimental observations.

In Haynes and Burton’s data [13], the apparent viscosity is observed to increase with R for constant Q experiments but decrease with R for constant Π experiments, in con-

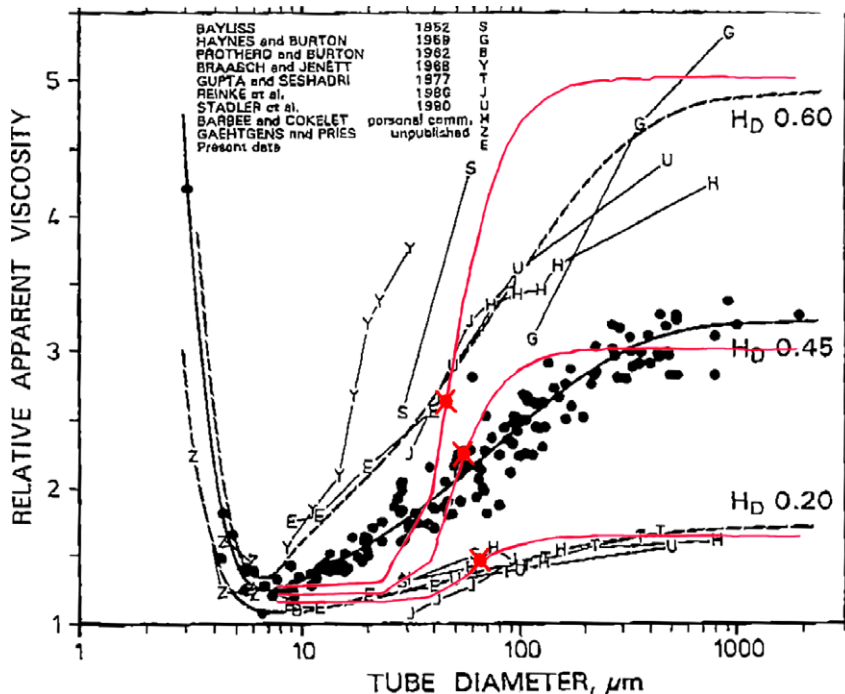


Fig. 8. Apparent blood viscosity in constant Q experiments of Haynes and Burton for various ϕ_0 and R . The computed curves are also shown. The crosses correspond to the onset of a clear marginal layer when the blood volume fraction is zero at the wall.

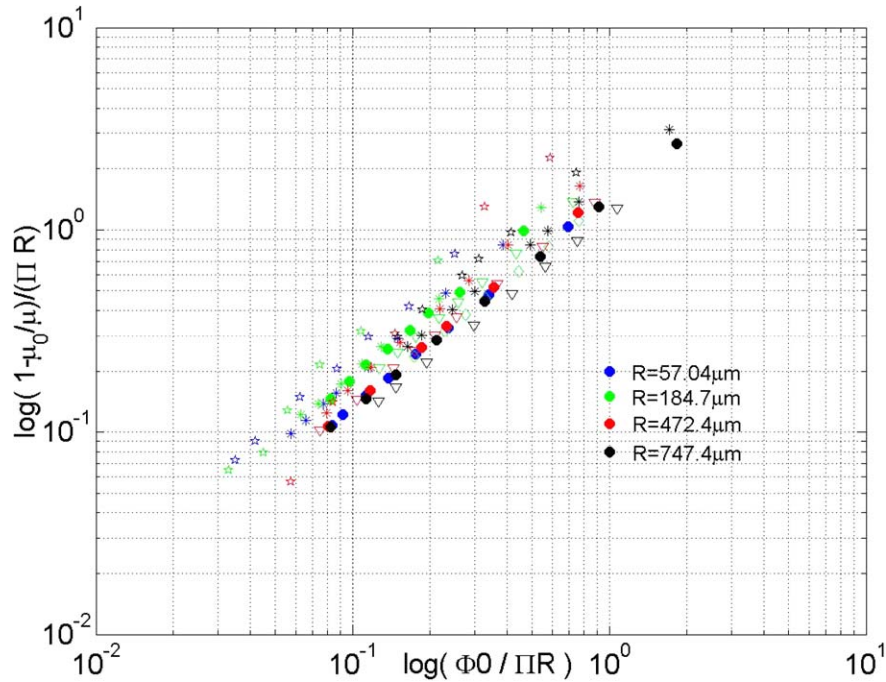


Fig. 9. Collapsed data of Haynes and Burton [13] for both constant pressure and constant flow rate whole blood flow in capillaries of radius R . The horizontal axis of $(\phi_0/\Pi R)$ has the same scaling as β .

tradition to the rigid particle result of (10). This apparent contradiction is explained by the β scaling of $\Pi R/\phi_0$ which introduces a new R scaling through Q in (10). In Fig. 9, we collapse all constant Π and constant Q data of Haynes and Burton [13] into a universal curve that depends only on $\phi_0/\Pi R$, the β scaling. The collapsed data span $0 < \phi_0 < 0.83$, $50 \mu\text{m} < R < 750 \mu\text{m}$ and $0 < \Pi < 160 \text{ mm H}_2\text{O}/\text{cm}$. This excellent collapse underscores the importance of deformation in blood rheology and the accuracy of our constitutive equations.

5. Corner deflection

The entrance deflection cannot be due to centrifugal force due to the small turning radius. Instead, we propose that it is due to a local but strong hydrodynamic interaction between the particles and the corner. The corner geometry, unlike the case of a flat wall, produces a curved flow field without fore-aft and cross-streamline symmetries about the particle. The stream function of a corner flow with the same flow rate $Q/2\pi R$ of the capillary flow could be solved as

$$\begin{aligned} \psi &= Q/2\pi R (r/R)^\lambda f(\lambda\theta) \\ &= (Q/2\pi R) (r/R)^\lambda [\cos((\lambda-2)\alpha) \cos \lambda\theta \\ &\quad - \cos(\lambda\alpha) \cos(\lambda-2)\theta], \end{aligned} \quad (11)$$

where f is a unit-order harmonic function of the azimuthal angle θ , and $\lambda = 1.56$ is the leading eigenvalue of the biharmonic operator for viscous flow near a wedge in cylindrical coordinates. The radial velocity $U_r \sim (Q/2\pi R^2)(r/R)^{\lambda-1} \times$

$f'(\lambda\theta)$ and azimuthal velocity $U_\theta \sim (Q/2\pi R^2)(r/R)^{\lambda-1} \lambda \times f(\lambda\theta)$ can be derived from this stream function. As $\lambda - 1$ is less than unity, the normal viscous stress due to U_r this flow exerts on an infinitesimally small particle at r becomes singular when r vanishes:

$$\tau_{rr} \sim 2\mu(Q/2\pi R^3)(r/R)^{\lambda-2}(\lambda-1)f'(\lambda\theta). \quad (12)$$

With this singular corner flow, the normal stress is clearly nonuniform in the r direction and hence, over a finite-size particle, a net force on the particle exists normal to the streamline. Using the particle radius a as a cut-off, this hydrodynamic interaction then produces a normal force F on the blood cell that scales as $\sim \mu a (a/R)^{\lambda-1} (Q/2\pi R^2)$.

Using Faxen law, the particle transverse deflection velocity [10] due to the normal pressure gradient can then be expressed as

$$V = Q/(6\pi R^2)(a/R)^{\lambda-1}. \quad (13)$$

This is the cross-streamline velocity due to hydrodynamic interaction with the corner. The radial cross-streamline deflection for the transit time across the corner can then be estimated as

$$b \sim (3/2\pi a/U_\theta)V \sim (\pi/2)a, \quad (14)$$

where $3/2\pi a/U_\theta$ is the circuit time around the corner, for a particle closes the surface. It is hence clear that the particle is deflected only a few particle diameters across the streamlines. This deflection difference is also independent of shear rate or flow rate, as is consistent with Fig. 6.

A contraction mapping of the streamlines at the corner onto the converged Poiseuille flow streamlines within the

capillary then gives an estimate of the deflected distance b from the wall in the capillary

$$b/R \sim (a/R)^\lambda. \tag{15}$$

With the deflected distance b , the particles need only migrate the reduced distance $(R - b)$ under the effect of shear-induced migration and the entrance transition length is

$$L_t \sim R(R - b)^2/\phi a^2. \tag{16}$$

With this corner deflection, the radial migration of blood cell deformation is enhanced. This produces a critical capillary radius that depends on ϕ_0 .

6. Meniscus packing region and critical penetration conditions

While radial migration and segregation of RBCs produce a lower apparent viscosity in well-developed and continuous capillary blood flow driven by a pump, they can have an opposite effect on wetting flow with an advancing meniscus. The radially segregated RBCs pack behind the meniscus as they possess a larger average speed than the meniscus speed. If the packing occurs near the entrance, the packed slug with elevated hydrodynamic resistance occupies a significant portion of the wetted length and can be longer than the length of the segregated region with lower apparent resistance. As such, capillary penetration is arrested. If the packing occurs far from the entrance, however, the lubricating and viscosity reducing effect of the dominant segregated region prevails.

The segregated RBCs behind the slug are held at the capillary axis by the shear-induced particle segregation mechanism that favors the low-shear axis over the high-shear wall region [5]. Due to RBC deformation, this shear-induced migration is much stronger for RBCs than rigid particles [15], thus explaining the lack of segregation in latex particle suspensions in Fig. 2. This migration mechanism can be interpreted as a negative diffusion process with a diffusivity of $\phi_0 \langle \gamma \rangle a^2$, where a is the effective blood cell radius ($\sim 5 \mu\text{m}$). This migration mechanism disappears at the meniscus, as the radial shear gradient disappears. Instead, a positive diffusion process due to radial concentration gradient develops to drive the blood cells to the wall with a diffusivity that also scales as $\phi_0 \langle \gamma \rangle a^2$ [5]. The slug length can hence be estimated by a balance between the radial diffusion time $R^2/\phi_0 \gamma a^2$ and the longitudinal convection time $L_{\text{slug}}/\langle u \rangle \sim L_{\text{slug}}/(R\gamma)$. This yields a L_{slug} whose R^3 scaling is in good agreement with our measured slug length in the insert of Fig. 10. There is a different ϕ_0 dependence through blood cell deformation [15] and we improve the above scaling empirically to $L_{\text{slug}} \sim 35.0(R^3/a^2)(\phi_0)^{1/2}$ to produce the good collapse of measured data for a wide range of blood cell concentrations and capillary radii in Fig. 10 insert.

Since L_{slug} is constant throughout the penetration, the blood accumulation rate in the slug is described by

$$d\phi_{\text{slug}}/dt = (\langle u\phi \rangle - \langle u \rangle \langle \phi \rangle) / L_{\text{slug}}, \tag{17}$$

where $\langle \cdot \rangle$ denotes cross-section average. A totally segregated suspension with all particles along the axis would yield an initial packing rate of $\langle u\phi \rangle - \langle u \rangle \langle \phi \rangle \sim \langle u \rangle \phi_0$ as the axis ve-

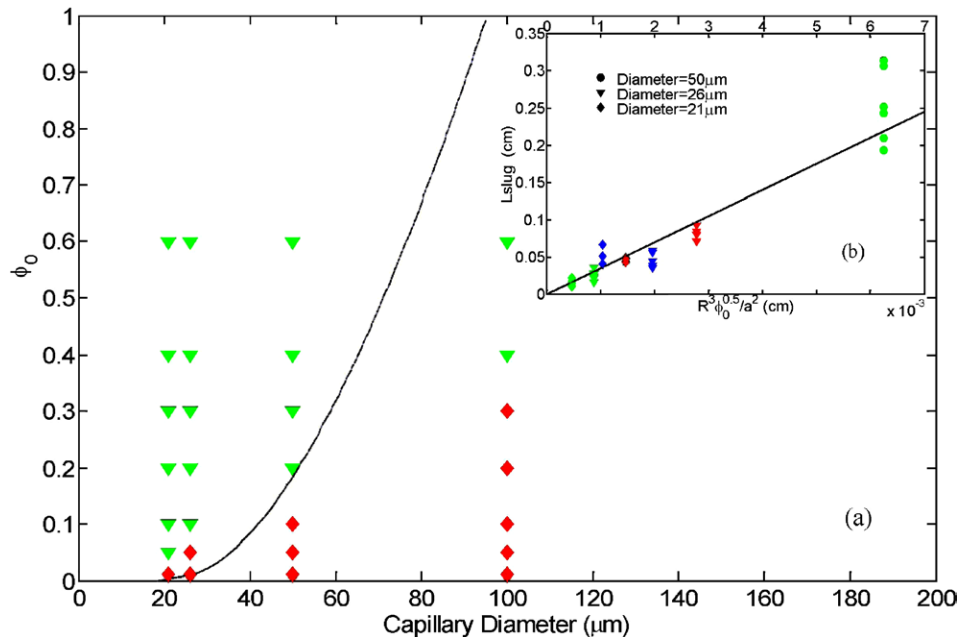


Fig. 10. Critical penetration condition in the concentration–diameter parameter space. The green triangles correspond to homogeneous wetting and the red diamonds arrested wetting due to the packing mechanism. The curve is our theoretical result. Insert measured slug length for three capillary diameters $D = 2R$ and three concentrations (red symbol 10%; blue symbol 5%; green symbol 1%) compared to our adjusted theoretical scaling, balancing rigid particle radial migration with longitudinal convection.

locity is twice the average velocity $\langle u \rangle$ in Poiseuille flow. With this approximation, (17) yields a correlation between the slug concentration ϕ_{slug} and the meniscus position (wetted length) L , $(\phi_{\text{slug}}/\phi_0) \sim (L/L_{\text{slug}})$. The wetted length L_{max} for the slug to reach maximum packing can hence be estimated by

$$L_{\text{max}} = L_{\text{slug}}/\phi_0 = 35.0(R^3/a^2)/\phi_0^{1/2}. \quad (18)$$

Combined with the other segregation mechanisms at the entrance, the segregated region is hence sandwiched between the entrance transition region and the concentrated meniscus slug. Failure to penetrate occurs when the segregated region is vanishing short and the maximum packing is reached as soon as the blood cells leave the entrance transition region,

$$L_{\text{max}} = L_t + L_{\text{slug}}. \quad (19)$$

If the entrance segregation is due to shear-induced migration, L_t would be identical to L_{slug} and (18) and (19) would produce the unreasonable penetration condition of $\phi_0 < 0.5$ independently of R , clearly in contradiction to Fig. 10. Corner deflection becomes negligible at large R and this purely shear-induced migration mechanism may be reached for large radii. Indeed, the data of Fig. 10 seem to approach a constant critical concentration of about 0.5 for $R > 100 \mu\text{m}$. However, we shall focus on the low-radii limit pertinent to microneedle designs, where the critical radius is a function of the concentration and vice versa. The deflection mechanism is hence responsible for the dependence of the penetration condition on capillary dimension.

Inserting (16) and (18) into (19), we obtain an estimate of the critical capillary radius R_c for penetration as a function of blood cell concentration ϕ_0 by expanding in ϕ_0

$$(R_c/a) = 1.77(1 + 1.04\phi_0^{1/4} + 1.38\phi_0^{1/2} + 1.97\phi_0^{3/4}), \quad (20)$$

which is in good agreement with the low-concentration data in Fig. 3a. The intercept $R_c = 1.77a \sim 10 \mu\text{m}$ at $\phi_0 = 0$ corresponds to $b = R$. This scaling prediction, which is in quantitative agreement with our critical capillary radius data for blood penetration in Fig. 8 predicts a critical capillary radius of $35 \mu\text{m}$ for whole blood ($\phi_0 = 0.45$). This invasion threshold is consistent with the industrial benchmark of $50 \mu\text{m}$.

7. Discussion

It is clear that RBC deformation is the key reason why meniscus packing and penetration failure occur. Although both rigid and deformable particles suffer from corner deflection, it is the latter that can retain the axial position at the entrance despite a large radial concentration gradient. Also, one means to remove deformation-induced segregation towards the axis is to reduce shear or increasing mixing. Electrokinetic flow is nearly shear-free and we indeed have been able to load blood into capillaries with $R < 20 \mu\text{m}$

with electrokinetic flow [19]. Microvortices to rehomogenize the blood cell distribution can also be utilized. Work is under way in our laboratory to produce microneedles that can circumvent blood loading failure with these strategies. Another approach is to reduce the corner deflection that enhances the radial migration effect at small capillary radii and high concentrations—the conditions most critical to diagnostic kits. Removal of this corner deflection could allow penetration of whole blood into any capillary larger than, say, $20 \mu\text{m}$ in radius. This may involve tedious modification of entrance geometry such as thickness of the capillary wall, angle of the corner, etc. The most promising solution, which may not be practical for some applications, is to mimic the blood-sucking mechanisms of a mosquito. The mosquito's proboscis is less than $100 \mu\text{m}$ in diameter and yet it suffers no blood penetration failure. The solution there, we believe, is the removal of the meniscus by preinjecting a second fluid from the mosquito. A robust microneedle that allows the loading of microliter of blood sample is the goal of our current efforts.

Acknowledgments

This work is supported by a NASA Grant NAG5-10503. We are grateful to Dmitri Lastochkin for assistance in collecting the data of Fig. 3 and to David T. Leighton and Ping Wang for valuable discussions and assistance. We also acknowledge the blood supply by Jason Gordon from Andre F. Palmer's group at Notre Dame.

References

- [1] V.V. Yuzhakov, D.V. McAllister, L. Olson, K.W. Leong, M. Teodorczyk, E. Kiser, U.S. Patent Application Publication (2002), no. US2002/0168290 A1.
- [2] P. Olla, Phys. Rev. Lett. 82 (1999) 453.
- [3] H.L. Goldsmith, S.G. Mason, J. Colloid Sci. 17 (1962) 448.
- [4] P.G. Saffman, J. Fluid. Mech. 22 (1965) 385.
- [5] D. Leighton, A. Acrivos, J. Fluid Mech. 181 (1987) 415.
- [6] A. Karnis, S.G. Mason, J. Colloid Interface Sci. 23 (1967) 120.
- [7] S. Kalliadasis, H.-C. Chang, IEC Res. 35 (1996) 2860.
- [8] E. Hrcir, J. Rosina, Physiol. Res. 46 (1997) 319.
- [9] R. Fahraeus, T. Lindqvist, Am. J. Physiol. 96 (1931) 562.
- [10] J. Happel, H. Brenner, Low Reynolds Number Hydrodynamics, Noordhoff, Leyden, 1973.
- [11] A.W. El-Kareh, T.W. Secomb, Int. J. Multiphase Flow 26 (2000) 1545.
- [12] A. Bellelli, P.L. Benedetti, M. Coletta, R. Ippoliti, M. Brunori, Biochem. Biophys. Res. Comm. 156 (1988) 970.
- [13] R.H. Haynes, A.C. Burton, Am. J. Physiol. 197 (1959) 943.
- [14] M. King, D. Leighton, Phys. Fluid 13 (2001) 397.
- [15] P.C.-H. Chan, L.G. Leal, J. Fluid Mech. 92 (1979) 131.
- [16] R.J. Phillips, R.C. Armstrong, R.A. Brown, Phys. Fluid A 4 (1992) 30–40.
- [17] K.D. Tachev, J.K. Angarska, K.D. Danov, P.A. Kralchevsky, Colloids Surf. B Biointerfaces 19 (2000) 61.
- [18] A.R. Pries, D. Neuhaus, P. Gaeltgens, Am. J. Physiol. 263 (1992) H1770.
- [19] A. Minerick, P. Takhistov, R. Zhou, H.-C. Chang, Electrophoresis 24 (2003) 3703.